nature

https://doi.org/10.1038/s41586-023-06745-7

Accelerated Article Preview

Low-loss contacts on textured substrates for inverted perovskite solar cells

Received: 28 June 2023

Accepted: 12 October 2023

Accelerated Article Preview
Published online: 23 October 2023

Cite this article as: Park, S. M. et al. Low-loss contacts on textured substrates for inverted perovskite solar cells. *Nature* https://doi.org/10.1038/s41586-023-06745-7 (2023)

So Min Park, Mingyang Wei, Nikolaos Lempesis, Wenjin Yu, Tareq Hossain, Lorenzo Agosta, Virginia Carnevali, Harindi R. Atapattu, Peter Serles, Felix T. Eickemeyer, Heejong Shin, Maral Vafaie, Deokjae Choi, Kasra Darabi, Eui Dae Jung, Yi Yang, Da Bin Kim, Shaik M. Zakeeruddin, Bin Chen, Aram Amassian, Tobin Filleter, Mercouri G. Kanatzidis, Kenneth R. Graham, Lixin Xiao, Ursula Rothlisberger, Michael Grätzel & Edward H. Sargent

Low-loss contacts on textured substrates for inverted perovskite solar cells

So Min Park[1,2,10], Mingyang Wei[3,10], Nikolaos Lempesis[4,10], Wenjin Yu[5], Tareq Hossain[6], Lorenzo Agosta[4], Virginia Carnevali[4], Harindi R. Atapattu[6], Peter Serles[7], Felix T. Eickemeyer[3], Heejong Shin[1], Maral Vafaie[2], Deokjae Choi[1], Kasra Darabi[8], Eui Dae Jung[2], Yi Yang[1], Da Bin Kim[2], Shaik M. Zakeeruddin[3], Bin Chen[1], Aram Amassian[8], Tobin Filleter[7], Mercouri G. Kanatzidis[1], Kenneth R. Graham[6], Lixin Xiao[5], Ursula Rothlisberger[4], Michael Grätzel[3]† & Edward H. Sargent[1,2,9]†

[1]Department of Chemistry, Northwestern University, Evanston, Illinois 60208, United States.

[2]Department of Electrical and Computer Engineering, University of Toronto, Toronto, Ontario, M5S 3G4, Canada.

[3]Laboratory of Photonics and Interfaces, Ecole Polytechnique Fédérale de Lausanne, Lausanne, 1015, Switzerland.

[4]Laboratory of Computational Chemistry and Biochemistry, Ecole Polytechnique Fédérale de Lausanne, Lausanne, 1015, Switzerland.

[5]State Key Laboratory for Artificial Microstructure and Mesoscopic Physics, Department of Physics, Peking University, Beijing 100871, P. R. China.

[6]Department of Chemistry, University of Kentucky, Lexington, KY, 40506, United States.

[7]Department of Mechanical and Industrial Engineering, University of Toronto, Toronto, Ontario, M5S 3G8, Canada.

[8]Department of Materials Science and Engineering, and Organic and Carbon Electronics Laboratories (ORaCEL), North Carolina State University, Raleigh, NC, 27695, United States.

[9]Department of Electrical and Computer Engineering, Northwestern University, Evanston, Illinois 60208, United States.

[10]These authors contributed equally to this work: So Min Park, Mingyang Wei, Nikolaos Lempesis

†e-mail: ted.sargent@northwestern.edu; michael.graetzel@epfl.ch

Inverted perovskite solar cells (PSCs) promise enhanced operating stability compared to their normal-structure counterparts[1–3]. To improve efficiency further, it is crucial to combine effective light management with low interfacial losses[4,5]. Here we develop a conformal self-assembled monolayer (SAM) as the hole-selective contact on light-managing textured substrates. Molecular dynamics simulations indicate cluster formation during phosphonic acid adsorption leads to incomplete SAM coverage. We devise a co-adsorbent strategy that disassembles high-order clusters, thus homogenizing the distribution of phosphonic acid molecules, thereby minimizing interfacial recombination and improving electronic structures. We report a lab-measured power-conversion efficiency (PCE) of 25.3% and a certified quasi-steady-state PCE of 24.8% for inverted PSCs, with a photocurrent approaching 95% of the Shockley-Queisser maximum. An encapsulated device having a PCE of 24.6% at room temperature retains 95% of its peak performance when stressed at 65°C and 50% relative humidity following >1000 hours of maximum power point tracking under 1-sun illumination. This represents one of the most stable PSCs subjected to accelerated ageing – achieved with a PCE surpassing 24%. The engineering of phosphonic acid adsorption on textured substrates offers a promising avenue for efficient and stable PSCs. It is also anticipated to benefit other optoelectronic devices that require light management.

Perovskite solar cells (PSCs) have recently attained a certified efficiency of 26.1%[6]; however, the very highest PCE devices have yet to meet operating stability under accelerated ageing tests[5]. The limited device stability is attributed to the presence of mobile and hygroscopic p-type dopants in hole-transporting layers, which undermine moisture and thermal stability[7]. Inverted PSCs present a solution by utilizing undoped hole-selective contacts[8]. Recent studies have shown PCEs surpassing 25% for inverted PSCs[2]. However, when adhering to the stringent quasi-steady-state (QSS) protocol, their certified efficiency (~24%) requires further improvement[3,9].

Efforts to improve inverted PSC efficiency have focused on interface passivation[2,9,10]. This approach suppresses non-radiative recombination and thus improves fill factors and photovoltages[11]. Nevertheless, higher photocurrents are needed for efficiency gains. In normal-structure PSCs, this has been realized using textured fluorine-doped tin oxides (FTO) as the transparent conductive oxides (TCO)[4,5]. The pyramidal grains on FTO minimize reflection losses and extend the length of the average optical path[4]. By contrast, inverted PSCs, often built on smooth indium tin oxides (ITO)[9,10], face substantial optical losses due to the lack of light management.

The discrepancy is ascribed to differences in transporting materials and deposition techniques. In normal-structure PSCs, inorganic hole-blocking layers are conformally deposited on textured substrates using spray pyrolysis and chemical bath deposition[4,5]. However, inverted PSCs typically employ ultra-thin (<5 nm) organic hole-selective contacts on substrates[2,3], which can be challenging to deposit uniformly using solution processing[12]. Inhomogeneity leads to energy losses and insufficient carrier extraction[13].

Self-assembled monolayers (SAMs), particularly those composed of phosphonic acid molecules with hole-selective tail groups, have shown promise in addressing this issue[14]. Phosphonic acids establish coordinative/covalent bonds with TCOs, allowing for sufficient SAM coverage on rough surfaces[15]. This could provide a low-loss interface, uniting light management with interface passivation. Indeed, photocurrent improvements have been observed when replacing SAM-modified ITO with FTO substrates in inverted PSCs[16].

Despite the promise, achieving a high-density, closely packed SAM remains challenging, which leads to erratic interfacial properties[17]. For example, M. Liu et al. revealed that phosphonic acids failed to fully cover textured wafers, which affected the performance of tandem solar cells[18]. Even

on flat substrates, the formation of SAMs tends to be non-uniform, a problem usually attributed to the limited solubility of phosphonic acids[19] and their insufficient chemical bond formation with metal oxides[20].

Several strategies have been proposed to ensure conformal SAM coverage, such as utilizing more reactive oxide surfaces (e.g., nickel oxides) to promote hetero condensation[18], employing thermal evaporation for SAM deposition[21], and designing highly soluble phosphonic acid molecules[19]. However, these methods can be laborious, requiring time-intensive molecule design, synthesis, and vacuum-based layer deposition. Additionally, the use of highly reactive oxides could compromise device stability due to redox reactions with ammonium halides[22].

Molecular dynamics simulations

We sought to deepen understanding of how phosphonic acids interact with textured TCOs. We began by looking at the case of 2-(9H-carbazol-9-yl)ethyl)phosphonic acid (2PACz), an organic molecule (Fig. 1a) capable of forming SAMs on TCOs[14], and investigated its interactions with FTO. 2PACz has found extensive applications as a hole-selective contact in PSCs in view of its excellent defect passivation and deep highest occupied molecular orbital (HOMO) level[21]. The surface properties of FTO were approximated using tin oxides (SnO_2), given that commercial FTO has a fluorine-doping level under 0.5% (atomic percentage)[23]. Flat vs. corrugated SnO_2 were analysed to understand the effects of surface morphology (Supplementary Fig. 1).

Molecular dynamics (MD) simulations suggest that 2PACz molecules can agglomerate, forming dimers, trimers, and tetramers (Fig. 1b and Supplementary Fig. 2). Within the initial 1 nanoseconds of simulations, 90% of the final number of clusters has been reached (Fig. 1b), and dimers were the most prevalent among clusters (Fig. 1c). Compared to flat surfaces, textured surfaces led to more clusters (e.g., 7 vs. 0 for 20 2PACz molecules on 6-nm-wide SnO_2) (Supplementary Note 1; Supplementary Figs. 3 and 4). The cluster formation is closely linked to the inhomogeneity of SAMs on FTO. For instance, when 162 2PACz molecules are positioned on top of textured SnO_2 surfaces, despite their initial random distribution (Supplementary Video 1), the finial equilibrated structures exhibit clear phase segregation (Fig. 1d), where almost 85% of the SnO_2 surface remains uncovered by any 2PACz molecules (Supplementary Fig. 5). These observations were also verified in a larger system (22-nm width; 1134 2PACz molecules) (Supplementary Fig. 6).

Reasoning that a thiol group (−SH) could interact with phosphonic acids, and a carboxyl group (−COOH) attached to FTO, we introduced 3-mercaptopropionic acid (3-MPA) (Fig. 1a) in simulations to break apart 2PACz clusters particularly on textured substrates. The approach is akin to the co-adsorbent strategy used in dye-sensitized solar cells to reduce dye aggregation on titanium oxides[24]. Similar strategies have been employed to improve the quality of hole-selective SAMs[25,26]. With 3-MPA at a molar ratio of 1:9 with 2PACz, we saw a relative 15% decrease in the number of clusters on textured surfaces (Fig. 1b), and a slower formation rate (20 ns^{-1} vs. 28 ns^{-1}) (Supplementary Fig. 7). In particular, the higher-order clusters (trimers and tetramers) decreased by 53% (Fig. 1c). As a result, the mixed system shows less phase segregation (Fig. 1e and Supplementary Video 2), leading to extended surface coverage (67% vs. 15%) by 2PACz molecules (Supplementary Fig. 5). Ab initio MD (AIMD) simulations (Supplementary Note 2 and Supplementary Fig. 8) indicate that the presence of 3-MPA hinders the free movement of individual 2PACz molecules by forming a supramolecular structure (Fig. 1f). This reduces agglomeration with already-formed dimers, suppressing the formation of higher-order clusters (Supplementary Video 3). Density functional theory (DFT) calculations revealed surface binding energies of −3.2 eV and −2.6 eV for 2PACz and 3-MPA, respectively, which are much stronger than the interaction energies of 2PACz clusters (−0.3 to −0.1 eV per molecule). This indicates robust anchoring of 2PACz and 3-MPA molecules upon contact with substrate surfaces.

Characterization of organic contacts

We deposited both 2PACz and a mixture of 2PACz:3-MPA on FTO substrates using solution processing, followed by annealing the film at 100°C and solvent washing (Methods). Micelles were detected in the processing solutions through dynamic light scattering (DLS) (Supplementary Fig. 9). However, due to their limited proportion in the volume distribution compared to 2PACz monomers, film formation primarily resulted from molecular diffusion rather than direct micellar adsorption[27].

The film composition and its interaction with FTO substrates were investigated using X-ray photoelectron spectroscopy (XPS) and attenuated total reflectance Fourier transform infrared spectroscopy (ATR-FTIR), respectively. For the film comprising solely 2PACz molecules (the control), the presence of 2PACz was evidenced by the appearance of the phosphine (P) doublet peak (Fig. 2a) and the characteristic C-N peak and C-C/C-H peak (Supplementary Fig. 10) in the

XPS spectra[21]. In the case of mixed film, 3-MPA was indicated by the sulfur (S) 2*p* doublet peak at around 163.8 eV (i.e., the thiol group) (Fig. 2a)[28]. From ATR-FTIR, bidentate or tridentate binding was identified as the mode of 2PACz-FTO interactions, given the appearance of the symmetric PO_3^{2-} stretching (at 996 cm^{-1} for the control sample)[29,30] and the disappearance of P–OH vibrations[14]. These also indicated that solvent washing removed unbound molecules[14]. With 3-MPA addition, a redshift of approximately 5 cm^{-1} was observed for the PO_3^{2-} vibrational mode, indicating the enhanced surface binding of 2PACz – as confirmed by AIMD simulations (Supplementary Note 3; Supplementary Figs. 11 and 12). ATR-FTIR of the FTO/3-MPA sample (Fig. 2b) further showed carboxylate-related peaks and a reduction in the intensity of the C=O peak, which correspond to the bidentate chelation of 3-MPA with FTO surfaces[31]. Combining the results from XPS and ATR-FTIR, we reasoned that 3-MPA functioned as a co-adsorbent, modulating the interaction of 2PACz with FTO substrates.

The resultant SAM uniformity was characterized by Kelvin probe force microscopy (KPFM). Topography images revealed that, despite varying SAM modifications, the surface morphology of FTO substrates was retained due to the ultra-thin nature of SAMs (Supplementary Fig. 13). From the respective contact potential difference (CPD) maps (Fig. 2c), we recorded surface potential variations on 2PACz-modified surfaces within a range of 120 mV. A Gaussian fit of the single peak in the CPD distribution yielded the full-width half-maximum (FWHM) of 37 mV (Supplementary Fig. 14). Introducing 3-MPA enhanced the homogeneity of electronic properties on SAM-modified surfaces, as reflected by a narrower CPD distribution with the FWHM of 22 mV.

To directly visualize the distribution of SAMs on FTO substrates, we performed high-angle annular dark-field (HAADF) scanning transmission electron microscopy (STEM) measurements. Fig. 2d shows cross-sectional HAADF-STEM images of both control and mixed samples. Because of the contrast in the atomic number[2], SAM was discernible as a dark layer sandwiched between the brighter FTO and protective molybdenum oxide (MoO_x) layers. For the control SAM, we observed thickness variations across the same FTO facet, with certain regions showing thicknesses less than 1 nm. This suggests a low-density coverage and inhomogeneous distribution of 2PACz molecules[32]. The mixed sample exhibited significant improvements in terms of SAM uniformity and coverage: A consistent thickness was recorded for the mixed SAM on the same facet, albeit

with variations between 1 and 2 nm across different facets. Correspondingly, mixed SAM-modified FTO substrates exhibited higher hydrophobicity than control SAM-modified counterparts (Supplementary Fig. 15). Cyclic voltammetry (CV) measurements further determined the areal density of 2PACz in the mixed SAM to be 3.9×10^{13} molecules cm^{-2}, a 70% increase from the 2.3×10^{13} molecules cm^{-2} in the control SAM (Supplementary Fig. 16)[16,27].

Characterization of perovskite films

To investigate the impact of SAMs on the structural and optoelectronic properties of perovskites, we fabricated triple-cation $Cs_{0.05}MA_{0.10}FA_{0.85}PbI_3$ perovskite thin films on different FTO/SAM substrates. From scanning electron microscopy (SEM), we observed no notable change in the perovskite surface morphology when 3-MPA was incorporated into the SAM (Fig. 3a, b). Grazing incidence wide-angle x-ray scattering (GIWAXS) measurements showed nearly identical crystal structures for perovskites deposited on both the control and mixed SAMs (Fig. 3c). Here, the main constituent was photoactive α-phase perovskites, with traces of the 4H hexagonal phase detected at $q = 0.82$ $Å^{-1}$ and 0.92 $Å^{-1}$ as well as PbI_2 at $q = 0.90$ $Å^{-1}$, respectively (Supplementary Fig. 14)[33]. Time-of-flight secondary ion mass spectrometry (TOF-SIMS) further confirmed that both 3-MPA and 2PACz molecules, due to their chemisorption on FTO surfaces, remained localized at the perovskite/FTO interfaces (Fig. 3d, e). These findings suggest that 3-MPA is not likely to change the perovskite formation process or contribute to the grain boundary or top surface passivation.

We conducted photoluminescence (PL) characterization by exciting perovskite thin films at a 1-sun-equivalent photon flux. We saw an average photoluminescence quantum yield (PLQY) of 0.13% ± 0.02% for perovskites directly deposited onto FTO substrates, corresponding to a quasi-Fermi level splitting (QFLS) of 1.105 eV (Supplementary Table 1)[34]. 2PACz can passivate defects on metal oxide surfaces and effectively block electron injection[35], resulting in an approximately 50-fold increase in the PL intensity (Fig. 3f). We noted an average PLQY of 7% ± 2% for the perovskite/2PACz/FTO stacks (Fig. 3g), corresponding to a QFLS of 1.207 eV. The incorporation of 3-MPA further improved the average PLQY to 10% ± 1%. This we ascribed to better SAM coverage rather than 3-MPA passivation since the thiol group of 3-MPA was embedded within the SAM (Fig. 1f).

We used ultraviolet and inverse photoelectron spectroscopy (UPS and IPES) to determine the work function and transport energy levels of perovskites and SAMs. The secondary electron cutoff in

192 the UPS spectra indicated an increase in the work function (WF) from 4.56 to 4.93 eV upon
193 depositing the control SAM on the FTO substrate (Supplementary Fig. 18). 3-MPA led to an
194 additional WF shift of +100 meV. The ionization energy (IE) was 5.51 and 5.64 eV for the control
195 and mixed SAMs, respectively. In contrast, perovskites exhibited similar conduction band
196 minimum (CBM) and valance band maximum (VBM) on different substrates (Fig. 3h). The
197 resultant energy level diagrams of perovskites and SAMs are depicted in Fig. 3i, j. A vacuum level
198 (VL) shift of 0.17 eV was recorded between the perovskite and the 2PACz bilayer, which further
199 increased to 0.32 eV for the perovskite/mixed-SAM bilayer[36]. A higher VL shift indicates an
200 enlarged built-in field[37], which in PSCs can lead to enhanced carrier extraction[38]. Meanwhile, the
201 IE offset between the bilayer remained consistent for the control and mixed SAMs (referenced to
202 the Fermi level (E_F)).

203 **Solar cell efficiency and stability**

204 We fabricated PSCs having the inverted structure: FTO/SAM/perovskites/3,4,5-trifluoroanilinium
205 (345FAn)/fullerene (C_{60})/bathocuproine (BCP)/Ag (Fig. 4a and Supplementary Fig. 19). 345FAn
206 was selected for interface engineering due to its thermal stability[1]. 2PACz (control) and 2PACz:3-
207 MPA (mixed) were employed as the SAMs for hole-selective contact. The corresponding solar
208 cell parameters are summarized in Fig. 4b. We found that compared to control devices, the mixed
209 SAM led to improved performance (average PCE 25.0% compared with 24.1%). This came from
210 open-circuit voltage (V_{oc}, from 1.141 V to 1.159 V) and fill factor (FF, from 82.3% to 84.1%)
211 (Supplementary Note 4). We noted that device reproducibility was comparable for both control
212 and mixed SAMs, likely due to SAM inhomogeneity occurring at the nanoscale[18,27]. The champion
213 device with the mixed SAM exhibited a PCE of 25.3% from the reverse *J-V* scan, which agrees
214 with the PCE obtained from the steady-state power output (Supplementary Fig. 20). The integrated
215 short-circuit current density (J_{sc}) of 25.8 mA cm^{-2} derived from the external quantum efficiency
216 (EQE) measurement matches well with that from the *J-V* sweep (Fig. 4c).

217 One mixed-SAM-based FTO device was characterized at Newport (Montana, USA); and produced
218 a QSS-certified PCE of 24.8%, with a V_{oc} of 1.150 V, a J_{sc} of 25.5 mA cm^{-2}, and an FF of 84.5%
219 (Fig. 4d and Supplementary Fig. 21). Although there have been reports of inverted PSCs with
220 efficiencies surpassing 25%[2,3], the certified PCEs measured under stabilized conditions (including
221 maximum power point (MPP) and QSS tracking) have yet to reach the same level (Supplementary

Table 2). The QSS efficiency reported herein represents a new record for inverted PSCs, improving upon the previous record QSS efficiency of 24.09% in literature (Fig. 4e).

For comparison, inverted PSCs were fabricated on smooth ITO substrates. We obtained an average PCE of 23.4% for control ITO devices, which was lower than that of control FTO devices, despite their higher average V_{oc} and FF (Supplementary Fig. 22). This emphasizes the need to augment J_{sc} for inverted PSCs. The limited J_{sc} is ascribed to the smoothness of ITO substrates (Supplementary Fig. 23), leading to reduced light-scattering and thus insufficient light absorption in the full device (Supplementary Fig. 24). Interestingly, the performance of mixed-SAM-based ITO devices was only slightly improved, possibly due to the weak interactions of 3-MPA with ITO surfaces (Supplementary Note 5; Supplementary Fig. 25).

We evaluated the operating stability of PSCs using International Summit on Organic Photovoltaic Stability (ISOS)-L-3 protocols, in which the encapsulated device was subjected to continuous 1-sun equivalent, white-LED illumination (Supplementary Fig. 26) at 50% relative humidity and heatsink temperature of 65°C. To impede ion and moisture diffusion, we replaced BCP with atomic-layer-deposited SnO_2 as a buffer layer[9]. The resultant device delivered a PCE of 24.6% at room temperature (Supplementary Fig. 27). During the ISOS-L-3 testing, the device initially demonstrated a PCE of 22.6%, which increased to 23.1% after 1.6 hours of MPP tracking (Fig. 4f). The lower PCE at 65°C, compared to room temperature, is ascribed to the negative temperature coefficient of PSCs (–0.15% /°C)[39]. The PCE stabilized at 21.9% (95% of the peak PCE) until the end of the test (1075 h), with the main degradation in the photocurrent (Supplementary Fig. 28). The initial performance and operating stability reported herein are compared with other PSCs subjected to ISOS-L-3 tests (Supplementary Table 3).

References

1. Park, S. M. *et al.* Engineering ligand reactivity enables high-temperature operation of stable perovskite solar cells. *Science* **381**, 209–215 (2023).

2. Zhang, S. *et al.* Minimizing buried interfacial defects for efficient inverted perovskite solar cells. *Science* **380**, 404–409 (2023).

3. Jiang, Q. *et al.* Surface reaction for efficient and stable inverted perovskite solar cells. *Nature* **611**, 278–283 (2022).

4. Kim, M. *et al.* Conformal quantum dot–SnO_2 layers as electron transporters for efficient perovskite solar cells. *Science* **375**, 302–306 (2022).

253 5. Park, J. *et al.* Controlled growth of perovskite layers with volatile alkylammonium chlorides.
254 *Nature* **616**, 724–730 (2023).

255 6. Best Research-Cell Efficiency Chart. *NREL* https://www.nrel.gov/pv/cell-efficiency.html
256 (2023).

257 7. You, S. *et al.* Radical polymeric p-doping and grain modulation for stable, efficient
258 perovskite solar modules. *Science* **379**, 288–294 (2023).

259 8. Zheng, X. *et al.* Managing grains and interfaces via ligand anchoring enables 22.3%-
260 efficiency inverted perovskite solar cells. *Nat. Energy* **5**, 131–140 (2020).

261 9. Chen, H. *et al.* Quantum-size-tuned heterostructures enable efficient and stable inverted
262 perovskite solar cells. *Nat. Photonics* **16**, 352–358 (2022).

263 10. Li, Z. *et al.* Organometallic-functionalized interfaces for highly efficient inverted perovskite
264 solar cells. *Science* **376**, 416–420 (2022).

265 11. Peng, W. *et al.* Reducing nonradiative recombination in perovskite solar cells with a porous
266 insulator contact. *Science* **379**, 683–690 (2023).

267 12. Camaioni, N. *et al.* Polymer solar cells with active layer thickness compatible with scalable
268 fabrication processes: a meta-analysis. *Adv. Mater.* **35**, 2210146 (2023).

269 13. Sahli, F. *et al.* Fully textured monolithic perovskite/silicon tandem solar cells with 25.2%
270 power conversion efficiency. *Nat. Mater.* **17**, 820–826 (2018).

271 14. Al-Ashouri, A. *et al.* Conformal monolayer contacts with lossless interfaces for perovskite
272 single junction and monolithic tandem solar cells. *Energy. Environ. Sci.* **12**, 3356–3369
273 (2019).

274 15. Paniagua, S. A. *et al.* Phosphonic acids for interfacial engineering of transparent conductive
275 oxides. *Chem. Rev.* **116**, 7117–7158 (2016).

276 16. Truong, M. A. *et al.* Tripodal triazatruxene derivative as a face-on oriented hole-collecting
277 monolayer for efficient and stable inverted perovskite solar cells. *J. Am. Chem. Soc.* **145**,
278 7528–7539 (2023).

279 17. Isikgor, F. H. *et al.* Molecular engineering of contact interfaces for high-performance
280 perovskite solar cells. *Nat. Rev. Mater.* **8**, 89–108 (2022).

281 18. Mao, L. *et al.* Fully textured, production-line compatible monolithic perovskite/silicon
282 tandem solar cells approaching 29% efficiency. *Adv. Mater.* **34**, 1–12 (2022).

283 19. He, R. *et al.* Improving interface quality for 1-cm^2 all-perovskite tandem solar cells. *Nature*
284 **618**, 80–86 (2023).

285 20. Phung, N. *et al.* Enhanced self-assembled monolayer surface coverage by ALD NiO in p-i-
286 n perovskite solar cells. *ACS Appl. Mater. Interfaces* **14**, 2166–2176 (2022).

287 21. Farag, A. *et al.* Evaporated self-assembled monolayer hole transport layers: lossless
288 interfaces in p-i-n perovskite solar cells. *Adv. Energy Mater.* **13**, 2203982 (2023).

22. Boyd, C. C. *et al.* Overcoming redox reactions at perovskite-nickel oxide interfaces to boost voltages in perovskite solar cells. *Joule* **4**, 1759–1775 (2020).

23. Fukano, T. Low-temperature growth of highly crystallized transparent conductive fluorine-doped tin oxide films by intermittent spray pyrolysis deposition. *Sol. Energy Mater Sol. Cells* **82**, 567–575 (2004).

24. Neale, N. R., Kopidakis, N., van de Lagemaat, J., Grätzel, M. & Frank, A. J. Effect of a coadsorbent on the performance of dye-sensitized tio_2 solar cells: shielding versus band-edge movement. *J. Phys. Chem. B* **109**, 23183–23189 (2005).

25. Deng, X. *et al.* Co-assembled monolayers as hole-selective contact for high-performance inverted perovskite solar cells with optimized recombination loss and long-term stability. *Angew. Chem. Int. Ed.* **134**, (2022).

26. Al-Ashouri, A. *et al.* Wettability improvement of a carbazole-based hole-selective monolayer for reproducible perovskite solar cells. *ACS Energy Lett.* **8**, 898–900 (2023).

27. Liu, M. *et al.* Compact hole-selective self-assembled monolayers enabled by disassembling micelles in solution for efficient perovskite solar cells. *Adv. Mater.* (2023) doi:10.1002/adma.202304415.

28. Love, J. C., Estroff, L. A., Kriebel, J. K., Nuzzo, R. G. & Whitesides, G. M. Self-assembled monolayers of thiolates on metals as a form of nanotechnology. *Chem. Rev.* **105**, 1103–1170 (2005).

29. Paniagua, S. A. *et al.* Phosphonic acid modification of indium–tin oxide electrodes: combined XPS/UPS/contact angle studies. *J. Phys. Chem. C* **112**, 7809–7817 (2008).

30. Hotchkiss, P. J., Malicki, M., Giordano, A. J., Armstrong, N. R. & Marder, S. R. Characterization of phosphonic acid binding to zinc oxide. *J. Mater. Chem.* **21**, 3107 (2011).

31. Nazeeruddin, M. K., Humphry-Baker, R., Liska, P. & Grätzel, M. Investigation of sensitizer adsorption and the influence of protons on current and voltage of a dye-sensitized nanocrystalline TiO_2 solar cell. *J. Phys. Chem. B* **107**, 8981–8987 (2003).

32. Bunker, B. C. *et al.* The impact of solution agglomeration on the deposition of self-assembled monolayers. *Langmuir* **16**, 7742–7751 (2000).

33. Dang, H. X. *et al.* Multi-cation synergy suppresses phase segregation in mixed-halide perovskites. *Joule* **3**, 1746–1764 (2019).

34. Caprioglio, P. *et al.* On the relation between the open-circuit voltage and quasi-fermi level splitting in efficient perovskite solar cells. *Adv. Energy Mater.* **9**, 1901631 (2019).

35. Al-Ashouri, A. *et al.* Monolithic perovskite/silicon tandem solar cell with >29% efficiency by enhanced hole extraction. *Science* **370**, 1300–1309 (2020).

36. Li, X. *et al.* Mapping the energy level alignment at donor/acceptor interfaces in non-fullerene organic solar cells. *Nat. Commun.* **13**, 2046 (2022).

37. Lami, V. *et al.* Visualizing the vertical energetic landscape in organic photovoltaics. *Joule* **3**, 2513–2534 (2019).

38. Sandberg, O. J. *et al.* On the question of the need for a built-in potential in perovskite solar cells. *Adv. Mater. Interfaces* **7**, 2000041 (2020).

39. Moot, T. *et al.* Temperature coefficients of perovskite photovoltaics for energy yield calculations. *ACS Energy Lett.* **6**, 2038–2047 (2021).

Figure Legends

Fig.1|MD simulations of phosphonic acid adsorption with and without molecular additives. **a**, Chemical structures of the phosphonic acid 2PACz and the bifunctional compound 3-MPA. **b**, Total number of 2PACz clusters formed over a set period, in the absence (control) and presence (mixed) of 3-MPA. **c**, Types of 2PACz clusters formed at equilibrium. **d, e**, Top views of equilibrated molecular representations of control (**d**) and mixed (**e**) systems. 2PACz and 3-MPA (where applicable) are shown in pink and blue, respectively; Sn and O atoms, shown in the background, are depicted in yellow and red, respectively. **f**, Successive steps along an AIMD trajectory showcasing the role of 3-MPA as a co-adsorbent. Large, encircled areas are magnifications of small ones.

Fig.2|Homogeneity of self-assembled monolayers formed on FTO substrates. **a**, XPS P 2*p* (left) and S 2*p* (right) spectra for the control and mixed samples. The peaks were fitted using one S 2*p* or P 2*p* doublet with a 2:1 peak area ratio. **b**, 2PACz (left) and 3-MPA (right) transmission FTIR spectra, compared with ATR-FTIR spectra for the SAM (left) and 3-MPA (right) coated FTO substrates. The FTIR peaks identified at 947 and 1021 cm^{-1} for 2PACz powders correspond to the symmetric and asymmetric stretching of P–OH, respectively. Cz = carbazole. **c**, KPFM images of control (left) and mixed (right) SAM-coated FTO substrates. **d**, Cross-sectional HAADF-STEM images of control (top) and mixed (bottom) SAMs sandwiched between MoO_x and FTO.

Fig.3|Materials properties of perovskite films on different FTO/SAM substrates. **a, b**, Top-view SEM images of perovskite films deposited on control (**a**) and mixed (**b**) SAMs. **c**, GIWAXS images for perovskite films on control (left) and mixed (right) SAMs. The color bar shows the diffraction intensity collected from the GIWAXS detector. q_{xy} and q_z represent in-plane and near out-of-plane scattering vectors, respectively. **d, e**, TOF-SIMS profiles of perovskites on FTO/control SAM (**d**) and FTO/mixed SAM (**e**) substrates measured in negative polarity. Traces of SH^- were identified at the perovskite/control SAM interface, possibly due to contamination of precursor materials. **f**, Absolute intensity PL spectra of perovskite films on bare FTO (no SAM) and control and mixed SAMs. **g**, PLQYs of perovskite films on control and mixed SAMs (5 samples for each condition). Statistical distribution represented in box plots (line within the box: mean, box limit: standard deviation). **h**, UPS and IPES spectra of perovskite films on control and mixed SAMs. Gaussian fit (grey line) was used to determine the conduction and valence bands. **i, j**, Schematic energy level diagrams of the perovskite/control SAM (**i**) and perovskite/mixed SAM bilayer (**j**), respectively.

Fig.4|Photovoltaic performance of perovskites solar cells. **a**, Schematic illustration of the device architecture with textured FTO substrate. **b,** Solar cell parameters for the control (16 devices) and mixed (32 devices) SAM devices. Statistical distribution represented in box-and-whisker plots (line within box: median, box limit: standard deviation, whiskers: 1.5 outliers). **c,** EQE and integrated J_{sc} (grey dashed line) curves of the mixed SAM device. **d,** QSS *J-V* curve of one representative mixed SAM device certified at Newport. Inset: PV parameters of the device. **e,** Certified performance of inverted PSCs measured under the QSS condition. **f,** MPP tracking of the encapsulated mixed SAM device at heatsink temperature of 65°C with a relative humidity of ~50% under 1-sun illumination. The device configuration is FTO/SAM/Perovskite/345FAn/C_{60}/ALD-SnO_2/Ag, having a PCE of 24.6% at room temperature.

Methods

Molecular dynamics simulations

Static DFT calculation and AIMD were performed with the CP2K[40] package utilizing a mixed Gaussian/plane wave (GPW) basis. The PBE exchange-correlation functional[41], DFT-D3 dispersion corrections[42], and dipole corrections[43] necessary for periodic boundary conditions along the perpendicular direction to the surface were included. Valence electron wave functions were expanded in a double-ζ Gaussian basis set with polarization functions (DZVP)[44]. The energy cut-off for the electron density expansion in the GPW method was 400 Ry. Born-Oppenheimer AIMD simulations were run with an integration time step of 0.5 fs and the system was kept at 300 K using the thermostat of Bussi et al.[45] in a canonical isothermal-isochoric (NVT) ensemble, where the total number of atoms N, the volume V and the temperature T of the system were held constant. All AIMD simulations were performed at Γ point. Being the most stable surface, the SnO_2 (110) was chosen as the substrate surface. The systems were equilibrated over 5 ps in the NVT ensemble and the remaining 40 ps were used for the production run. To investigate the interactions between the 2PACz and 3-MPA molecules, as well as molecules and the SnO_2 substrate, 5 scenarios were simulated: (1) a single molecule (2PCAz or 3-MPA) on SnO_2 (110), (2) one 2PACz and one 3-MPA concurrently on SnO_2 (110), (3) two 2PACz and one 3-MPA on SnO_2(110), (4) four 2PACz and one 3-MPA on SnO_2(110), and (5) six 2PACz and one 3-MPA on SnO_2 (110). In all the scenarios, an in-plane SnO_2 (110) simulation cell of 22.690 Å × 27.756 Å with 45 Å of vacuum between the slab repetitions was used. AIMD was also used to estimate the interaction energy of 2PACz and 3-MPA with the SnO_2 (110) surface. The final AIMD configurations were relaxed with DFT to extract the interaction energies of the molecules. Binding energies were calculated as $\Delta E_b = E_{tot} - E_S - E_{mol}$, where E_{tot} is the energy of the final relaxed configuration (molecule on SnO_2 (110)); E_S is the energy of the final configuration of the slab; E_{mol} is the energy of the final configuration of the isolated molecule. The interaction energies of 2PACz clusters were computed after DFT relaxations of isolated clusters. Dimers, trimers, and tetramers were considered. Interaction energies per molecule were calculated as $\Delta E_i = (E_{tot} - nE_{mol})/n$, where E_{tot} is the energy of the final relaxed cluster; n is the number of molecules forming the cluster; E_{mol} is the energy of a single relaxed molecule assumed isolated. Vibrational power spectra were computed as the Fourier transform of the autocorrelation function of the atomic velocities.

Classical MD simulations with full atomic resolution were realized with the help of the LAMMPS MD simulator[46]. The equations of motion were integrated using the Velocity-Verlet method[47], with a 1 fs time step, while bond stretching was not constrained for any bonds. To maintain isothermal conditions, the deterministic Nosé – Hoover thermostat[48,49], with a time constant equal to 0.1 ps, was utilized. This ensured that thermostating was applied to both translational and rotational degrees of freedom, crucial for the asymmetric 2PACz and 3-MPA molecules. All classical MD simulations were realized in the canonical NVT ensemble at T = 300K comprising a V-shaped SnO_2 (110) model system with dimensions 60 Å × 105 Å × 40 Å. Periodic boundary conditions were used in x- and y-directions, whereas reflective boundary conditions were employed in the z-direction. The two considered systems, control and mixed, comprised a total of 18498 and 18714 atoms, respectively, whereas the experimental molar ratio (2PACz/3-MPA= 9/1) was retained in the simulated mixed system. The systems were equilibrated for 1 ns followed by a 10ns production simulation, where sampling took place every 500 fs for the calculation of ensemble averages. A snapshot of the system was taken every 1000 fs for visualization purposes. The calculation of the number distributions of formed 2PACz clusters was performed through an in-house code utilizing

418 a threshold distance of 8 Å among the centre of masses of adjacent 2PACz molecules in accordance
419 with the nearest neighbour shell of the corresponding radial distribution function as clustering
420 criterion.

421 To accurately capture the interactions of SnO_2, the thoroughly validated classical force field
422 developed by Bandura et al.[50] was used. The all-atom OPLS force field was utilized for 3-MPA,
423 wherein the corresponding interaction parameters were obtained with the help of the LigParGen
424 server[51]. For 2PACz, containing the phosphonic functional group, the specially designed force field
425 developed by Meltzer et al.[52] based on the Generalized Amber Force Field[53] was utilized. The van
426 der Waals and electrostatic non-bonded interactions were calculated using a real-space cutoff
427 radius of 10 Å and 8 Å, respectively, whereas the particle-particle-particle-mesh (PPPM) scheme[54]
428 with an accuracy of 0.0001 (kcal/mol)/Å was used for the consideration of long-range electrostatic
429 interactions. Because the SnO_2 force field uses a Buckingham potential for the van der Waals
430 interactions, its combination with the Lennard-Jones potential used for the compounds was
431 realized by fitting the Buckingham parameters of SnO_2 to a suitable set of Lennard-Jones
432 parameters[55] and geometric mixing rules were applied for all dissimilar non-bonded interactions.

433 **Materials**

434 All materials were used as received without further purification. Organic halide salts, including
435 methylammonium iodide (MAI), formamidinium iodide (FAI), methylammonium chloride
436 (MACl), were purchased from Great Cell Solar. Cesium iodide (CsI), 3-mercaptopropionic acid
437 (3-MPA), 3,4,5-trifluoroaniline (98%), and guanidinium thiocyanate (GuaSCN) were purchased
438 from Sigma-Aldrich. 3,4,5-trifluoroaniline was converted to its ammonium form following the
439 published procedure. [2-(9H-Carbazol-9-yl)ethyl]phosphonic Acid (2PACz), lead iodide (PbI_2,
440 99.99%), and bathocuproine (BCP) were purchased from TCI. Anhydrous solvents including N,
441 N-dimethylformamide (DMF, 99.8%), dimethyl sulfoxide (DMSO, 99.9%), 2-propanol (IPA,
442 99.5%), chloroform (CF, 99.8%), and anisole (99.7%) were purchased from Sigma-Aldrich. C_{60}
443 was purchased from Xi'an Polymer Light Technology Corp. ITO and FTO (TEC 10) substrates
444 were purchased from Thin Film Devices Inc. and Ossila, respectively.

445 **Perovskite film fabrication**

446 1.5 M of $Cs_{0.05}MA_{0.1}FA_{0.85}PbI_3$ perovskite precursor was fully dissolved in mixed solvents of DMF
447 and DMSO (4:1, v/v) with the molar ratio for FAI/MAI/CsI was 0.85:0.1:0.05. 10 mg mL^{-1} MACl
448 and 8 mg mL^{-1} GuaSCN were added in the solution to improve the film morphology. The precursor
449 solution was filtered through a 0.22 μm polytetrafluoroethylene (PTFE) membrane before use. 60
450 μL of perovskite solution was deposited on the substrate and spun cast at 1000 rpm for 10 s
451 followed by 6000 rpm for 30 s. 150 μL anisole was dropped onto the substrate during the last 5 s
452 of the spinning, resulting in the formation of dark brown films that were then annealed on a hot
453 plate at 100°C for ITO and 120°C for FTO for 20 min.

454 **Device fabrication**

455 FTO glasses were sequentially sonicated in aqueous detergent, deionized water, acetone, and IPA
456 each for 10 min. After drying with nitrogen, the substrates were exposed to UV-ozone treatment
457 for 15 min to remove organic contaminants and then transferred into a nitrogen-filled glovebox
458 maintaining less than 0.1 ppm of O_2 and H_2O. 100 μL of 2PACz or a mixture of 2PACz:3-MPA (in
459 a molar ratio of either 9:1 in characterization and device fabrication, or 8:2 in XPS measurements)

in anhydrous ethanol (1 mM) solution was uniformly spread on the substrates and allowed to rest for 15 s, followed by spinning the films at 3000 rpm for 30s. The films were then annealed at 100°C for 10 min and washed by dropping 500 μL ethanol during the film spinning at 3000 rpm. Perovskites solution was deposited on the SAM-modified substrate as detailed above. 200 μL of 345FAn solution (1 mg/mL) in CF with an additional 3% of IPA was then drop cast within 2-3 s on the perovskite film spinning at 4000 rpm (i.e., dynamic spinning) and annealed at 100°C for 5 min. Both control and mixed SAM films were then transferred to the thermal evaporator (Angstrom engineering). C_{60} (30 nm) and BCP (7 nm) were deposited sequentially with a rate of 0.3 Å s^{-1} and 0.5 Å s^{-1}, respectively, at a pressure of ca. 2 x 10^{-6} mbar. Finally, Ag contact (140 nm) was deposited on top of BCP through a shadow mask with the desired aperture area. For the stability testing, ALD-SnO_2 were used as the barrier layer. The deposition of ALD-SnO_2 was carried out in the PICOSUN R-200 Advanced ALD system. H_2O and TDMASn were used as oxygen and tin precursors. Precursor and substrate temperature were set to 75°C and 85°C, respectively. 90 SCCM N_2 was used as carrier gas. Pulse and purge times for H_2O were 1 s and 5 s, and 1.6 s and 5 s for TDMASn. The total deposition cycle is 120, corresponding to 20 nm of SnO_2.

Solar cell characterization

The current-voltage (*I-V*) characteristics of solar cells were measured using a Keithley 2400 sourcemeter under the illumination of solar simulator (Newport, Class AAA) at the light intensity of 100 mW cm^{-2} as checked with a calibrated reference solar cell (Newport). The stabilized PCE was measured by setting the bias voltage to the V_{MPP} and then tracing the current density. The V_{MPP} was determined from the reverse *I-V* curve. The active area was determined by the aperture shade mask (0.049 cm^2) placed in front of the solar cell to avoid overestimation of the photocurrent density. EQE spectra were recorded with a commercial system (Arkeo-Ariadne, Cicci Research s.r.l.) based on a 300 W xenon light source and a holographic grating monochromator (Cornerstone, Newport).

Stability tests of solar cells

Devices were placed in a homemade stability tracking station. The illumination source is a white light LED with intensity calibrated to match the 1-sun condition. For the ISOS-L-3 ageing protocol (65 or 85°C; 50% relative humidity; MPP)[56], the device chamber was left open in a room with 50±10% humidity and solar cell was mounted on a metal plate kept at 65°C by a heating element. A thermal couple attached to the metal plate was used to monitor and provide feedback control to the heating element to ensure temperature consistency. MPP was tracked using a home-build MATLAB-based MPP tracking system using a 'perturb and observe' method. The MPP was updated every 1000 minutes. Encapsulation was done by capping the device with a glass slide, using UV-adhesive (Lumtec LT-U001) as a sealant.

XPS measurements

XPS measurements were performed with a Thermo Scientific K-Alpha system with 180° double-focusing, hemispherical analyser. The system is equipped with a 128-channel detector and monochromatic small spot XPS. An Al Kα source (1486.6 eV) was used for excitation and a pass energy of 50 eV was used for XPS acquisition. Samples mounted on a metal specimen holder. All data were analysed with CasaXPS and Thermo Avantage software.

KPFM measurements

KPFM measurements were performed using an Asylum Research Cypher S atomic force microscope (Oxford Instruments, Santa Barbara, USA) with an ASYELEC.01-R2 Ti-Ir coated cantilever (Asylum Research). Scans were performed over 2 μm at 512 pixels and 0.5 Hz using a two-pass method where the first pass is a tapping mode topography scan and the second in KPFM mode with a tip potential of 3 V and a surface clearance of 5 nm. Cantilever calibration was performed using the Thermal method from the Asylum Research GetReal database.

HAADF-TEM measurements

HAADF-TEM images were acquired at an aberration corrected FEI (Titan Cubed Themis G2) operated at 300 kV equipped with an XFEG gun and Bruker Super-X EDS detectors. The SAM samples had a structure of glass/FTO/SAM/MoO_x (50 nm), where the MoO_x layer was deposited through thermal evaporation with a low rate of 0.1 Å s^{-1} at a pressure below 2 x 10^{-4} Pa. The cross-sectional samples were prepared by using a focused ion beam system (FIB, Helios G4 UX). Another protective layer of carbon was thermally evaporated before ion-beam cutting and etching.

CV measurements

CV measurements were conducted using a three-electrode configuration with a potentiostat (PGSTAT204, Autolab). The working electrodes were prepared using a spin coating method on an FTO electrode. The exposed area of the working electrode to the electrolyte measures 8 mm × 21.4 mm. A platinum plate and an Ag/AgCl electrode (in a 3.0 M KCl solution) were employed as the counter and reference electrodes, respectively. The measurements were performed in an Ar-saturated solution of 1,2-dichlorobenzene (o-DCB) with 0.1 M tetrabutylammonium hexafluorophosphate ($TBA^+PF_6^-$) serving as the supporting electrolyte. All potentials are referenced against the ferrocene redox couple, serving as an internal standard. The effective coverage of the self-assembled monolayers on the FTO surface is measured by the slope of a linear dependency of the oxidative peak intensity against the scan rate as follows:

$$i_{p,o} = \frac{n^2 F^2}{4RTN_A} A\Gamma^* v$$

$i_{p,o}$ is the oxidative peak current, v is the voltage scan rate, n is the number of electrons transferred, F is the Faraday constant (96,485 C mol^{-1}), R is the universal gas constant (8.314 J K^{-1} mol^{-1}), T is the temperature, N_A is the Avogadro constant, A is the electrode area, and Γ^* is the areal density.

UPS and IPES measurements

UPS measurements were taken with an Excitech H Lyman-α photon source (10.2 eV) with a nitrogen-filled beam path coupled with a PHI 5600 UHV and analyser system. A sample bias of -5 V was applied and a pass energy of 5.85 eV was used for UPS acquisition. IPES measurements were performed in the Bremsstrahlung isochromatic mode with electron kinetic energies below 5 eV and an electron gun emission current of 2 μA was used to minimize sample damage. A Kimball Physics ELG-2 electron gun with a BaO cathode was used to generate the electron beam. Emitted photons were collected with a bandpass photon detector consisting of an optical bandpass filter (254 nm, Semrock) and a photomultiplier tube (R585, Hamamatsu Photonics). Samples were held at a -20 V bias during all IPES measurements and the UHV chamber was completely dark.

Other characterizations

Particle size distributions in solutions were determined by the DLS technique using a Malvern Zetasizer Nano ZS. Contact angles were measured using VCA-Optima XE. The image was taken with CCD camera within 1 s after water droplet. GIWAXS measurements were performed at CMS beamline, NSLS II. The monochromatic X-ray with the energy of 13.5 keV shone upon the samples at different grazing incident angles of 1°, 0.5°, and 0.08° with an exposure time of 10 s. A Pilatus800K detector was placed 259 mm away from the sample to capture the 2D diffraction pattern. Absolute intensity photoluminescence spectra were measured using an integrating sphere, and Andor Kymera 193i spectrograph, and a 660 nm continuous-wave laser set at 1-sun equivalent photon flux (1.1 μm beam full-width half-maximum, 632 μW); photoluminescence was collected at normal incidence using a 0.1 NA, 110 μm-diameter optical fiber. TOF-SIMS was conducted on the IONTOF M6 instrument with a Bi^{3+} (30 keV) primary ion beam for analysis and an Cs-cluster gun (2 keV) for sputtering. Data was acquired in positive mode with an analysis area of 49 × 49 μm^2 centred and a raster area of 200 × 200 μm^2. IR spectra were obtained in the attenuated total reflectance mode using a Fourier-transform IR spectrometer (Thermo Scientific iS50). Samples were prepared on the FTO substrate and scanned in the spectral range of 4000 to 550 cm^{-1} with a minimum number of 500 scans and a resolution of 4 cm^{-1}. The triangular apodization function was used to improve the signal-to-noise ratio. High-resolution SEM images were obtained using the Hitachi S5200 microscope with an accelerating voltage of 1.5 kV. A low accelerating voltage and a low beam current were deployed to reduce surface damage of perovskite films under electron beam bombardment. The diffuse and specular light reflected from the substrate surface was measured using a Cary 5000 UV-Vis-NIR double-beam spectrophotometer in diffuse reflectance mode. Pure $BaSO_4$ was used for the baseline collection.

Additional References

40. Kühne, T. D. *et al.* CP2K: An electronic structure and molecular dynamics software package - Quickstep: Efficient and accurate electronic structure calculations. *J. Chem. Phys.* **152**, 194103 (2020).

41. Van Setten, M. J. *et al.* The PseudoDojo: Training and grading a 85 element optimized norm-conserving pseudopotential table. *Comput. Phys. Commun.* **226**, 39–54 (2018).

42. Grimme, S. Density functional theory with London dispersion corrections. *Wiley Interdiscip. Rev. Comput. Mol. Sci.* **1**, 211–228 (2011).

43. Bengtsson, L. Dipole correction for surface supercell calculations. *Phys. Rev. B* **59**, 12301–12304 (1999).

44. VandeVondele, J. & Hutter, J. Gaussian basis sets for accurate calculations on molecular systems in gas and condensed phases. *J. Chem. Phys.* **127**, 114105 (2007).

45. Bussi, G., Donadio, D. & Parrinello, M. Canonical sampling through velocity rescaling. *J. Chem. Phys.* **126**, 014101 (2007).

46. Kryuchkov, N. P., Yurchenko, S. O., Fomin, Y. D., Tsiok, E. N. & Ryzhov, V. N. Complex crystalline structures in a two-dimensional core-softened system. *Soft Matter.* **14**, 2152–2162 (2018).

47. Swope, W. C., Andersen, H. C., Berens, P. H. & Wilson, K. R. A computer simulation method for the calculation of equilibrium constants for the formation of physical clusters of molecules: Application to small water clusters. *J. Chem. Phys.* **76**, 637–649 (1982).

48. Nosé, S. A unified formulation of the constant temperature molecular dynamics methods. *J. Chem. Phys.* **81**, 511–519 (1984).

49. Kassir, Y., Kupiec, M., Shalom, A. & Simchen, G. Cloning and mapping of CDC40, a Saccharomyces cerevisiae gene with a role in DNA repair. *Curr. Genet.* **9**, 253–257 (1985).

50. Bandura, A. V., Sofo, J. O. & Kubicki, J. D. derivation of force field parameters for SnO_2 $-H_2O$ surface systems from plane-wave density functional theory calculations. *J. Phys. Chem. B* **110**, 8386–8397 (2006).

51. Dodda, L. S., Cabeza de Vaca, I., Tirado-Rives, J. & Jorgensen, W. L. LigParGen web server: an automatic OPLS-AA parameter generator for organic ligands. *Nucleic Acids Res.* **45**, W331–W336 (2017).

52. Meltzer, C. *et al.* indentation and self-healing mechanisms of a self-assembled monolayer—a combined experimental and modeling study. *J. Am. Chem. Soc.* **136**, 10718–10727 (2014).

53. Wang, J., Wolf, R. M., Caldwell, J. W., Kollman, P. A. & Case, D. A. Development and testing of a general amber force field. *J. Comput. Chem.* **25**, 1157–1174 (2004).

54. Hockney, R. W. & Eastwood, J. W. *Computer Simulation Using Particles*. (CRC Press, 2021). doi:10.1201/9780367806934.

55. Lim, T.-C. Alignment of Buckingham parameters to generalized Lennard-Jones potential functions. *Zeitschrift für Naturforschung A* **64**, 200–204 (2009).

56. Khenkin, M. V. *et al.* Consensus statement for stability assessment and reporting for perovskite photovoltaics based on ISOS procedures. *Nat. Energy* **5**, 35–49 (2020).

Acknowledgements

This research was made possible by the U.S. Department of the Navy, Office of Naval Research Grant (N00014-20-1-2572). This work was supported in part by Ontario Research Fund-Research Excellence program (ORF7-Ministry of Research and Innovation, Ontario Research Fund-Research Excellence Round 7). This work was also supported under award number OSR-CRG2020-4350.2. M.W. acknowledges funding from the European Union's Horizon 2020 Research and Innovation program under the Marie Skłodowska-Curie Grant Agreement No. 101026353. T.H., H.R.A., and K.R.G. gratefully acknowledge funding from the National Science Foundation under award no. DMR-2102257. L.X. acknowledges support by National Natural Science Foundation of China (no. 61935016, 52173153) and the Electron Microscopy Laboratory of Peking University for the use of electron microscopes. M.G.K. acknowledges support by the

Office of Naval Research under award number N00014-20-1-2725. A.A. acknowledges support by the Office of Naval Research under award number N00014-20-1-2573. P.S. acknowledges the support of the Vanier Canada Graduate Scholarship. This work made use of the NUFAB and Keck-II facilities of Northwestern University's NUANCE Center, which has received support from the SHyNE Resource (NSF ECCS-2025633), the IIN, and Northwestern's MRSEC program (NSF DMR-1720139). We thank Damir Kopilovic for providing the LED spectrum and Jing Gao for assisting with the SEM measurements.

Author contributions

S.M.P., M.W., M.G., and E.H.S. conceived the idea and proposed the experimental and modelling design. N.L., L.A., V.C., and U.R. carried out the MD simulation. S.M.P. fabricated all the devices and conducted the characterization. T.H., H.R.A and K.R.G performed XPS, UPS, and IPES characterization and data analysis. W.Y. and L.X. carried out the HAADF-STEM measurements. F.T.E., M.W., S.M.Z., and M.G. conducted the PL and EQE characterization and data analysis. M.W. measured DLS. H.S. conducted CV measurements and data analysis. D.C. performed UV-Vis spectroscopy characterization. Y.Y. and M.G.K. measured TOF-SIMS. K.D. and A.A. performed the GIWAXS measurements. M.V., E.D.J. and D.B.K. helped with the device fabrication and material characterization. P.S. and T.F. performed the KPFM measurements. M.W., S.M.P., N.L., M.G., and E.H.S. co-wrote the manuscript. All authors contributed to data analysis, read, and commented on the manuscript.

Competing interests

The authors declare no competing interests.

Data availability

All data are available in the main text or the supplementary materials. Further data are available from the corresponding author on reasonable request.

Code availability

The codes and post-analysis tools for MD simulations are available in the following repository: https://doi.org/10.5281/zenodo.8393081.

Correspondence and requests for materials should be addressed to M.G. or E.H.S.

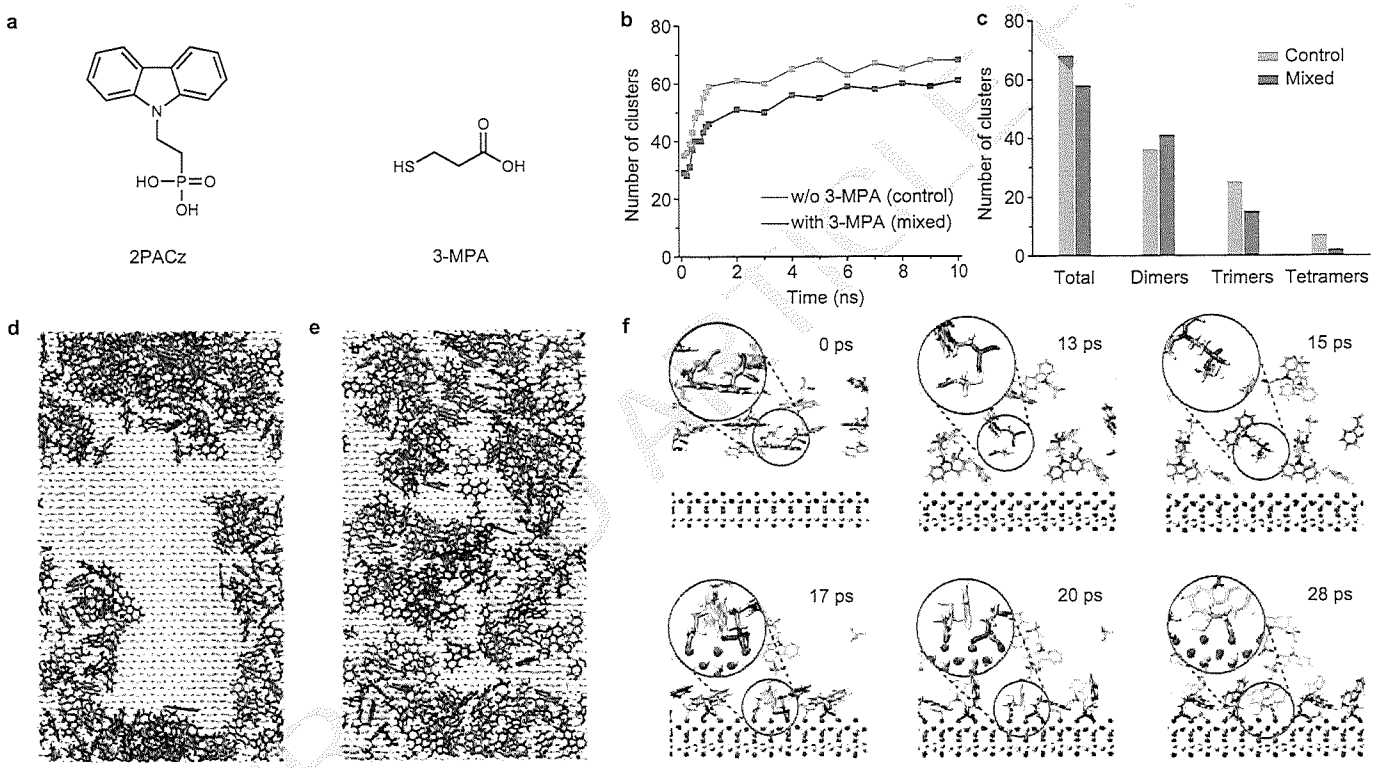
a
2PACz
3-MPA
b
Number of clusters
Time (ns)
w/o 3-MPA (control)
with 3-MPA (mixed)
c
Number of clusters
Control
Mixed
Total
Dimers
Trimers
Tetramers
d
e
f
0 ps
13 ps
15 ps
17 ps
20 ps
28 ps

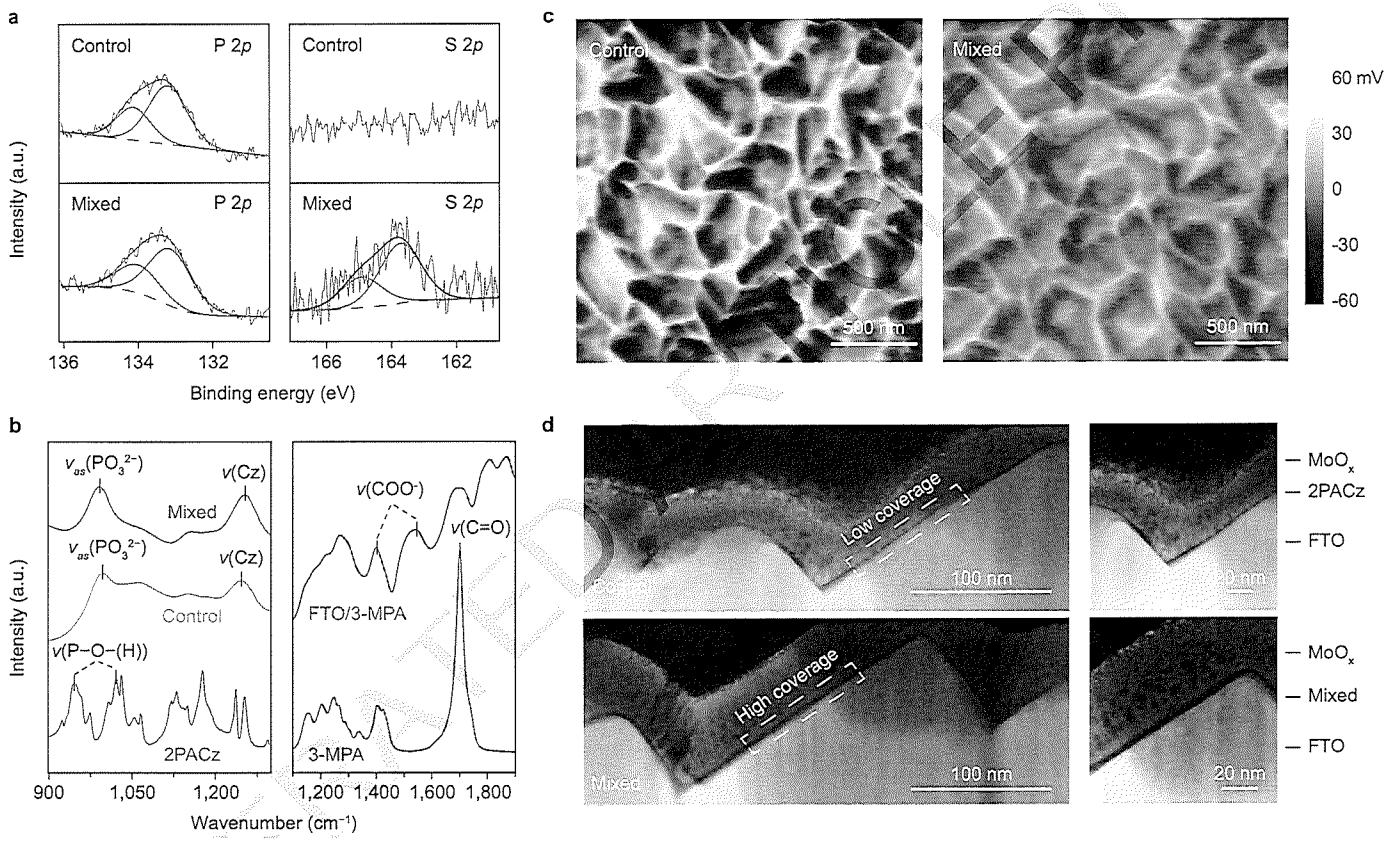
a
Control
P 2p
Control
S 2p
Mixed
P 2p
Mixed
S 2p
Intensity (a.u.)
136
134
132
166
164
162
Binding energy (eV)
b
$\nu_{as}(PO_3^{2-})$
ν(Cz)
Mixed
$\nu_{as}(PO_3^{2-})$
ν(Cz)
Control
ν(P–O–(H))
2PACz
ν(COO⁻)
ν(C=O)
FTO/3-MPA
3-MPA
Intensity (a.u.)
900
1,050
1,200
1,200
1,400
1,600
1,800
Wavenumber (cm⁻¹)
c
Control
500 nm
Mixed
500 nm
60 mV
30
0
-30
-60
d
Low coverage
100 nm
Control
MoO_x
2PACz
FTO
High coverage
100 nm
Mixed
MoO_x
Mixed
FTO
20 nm

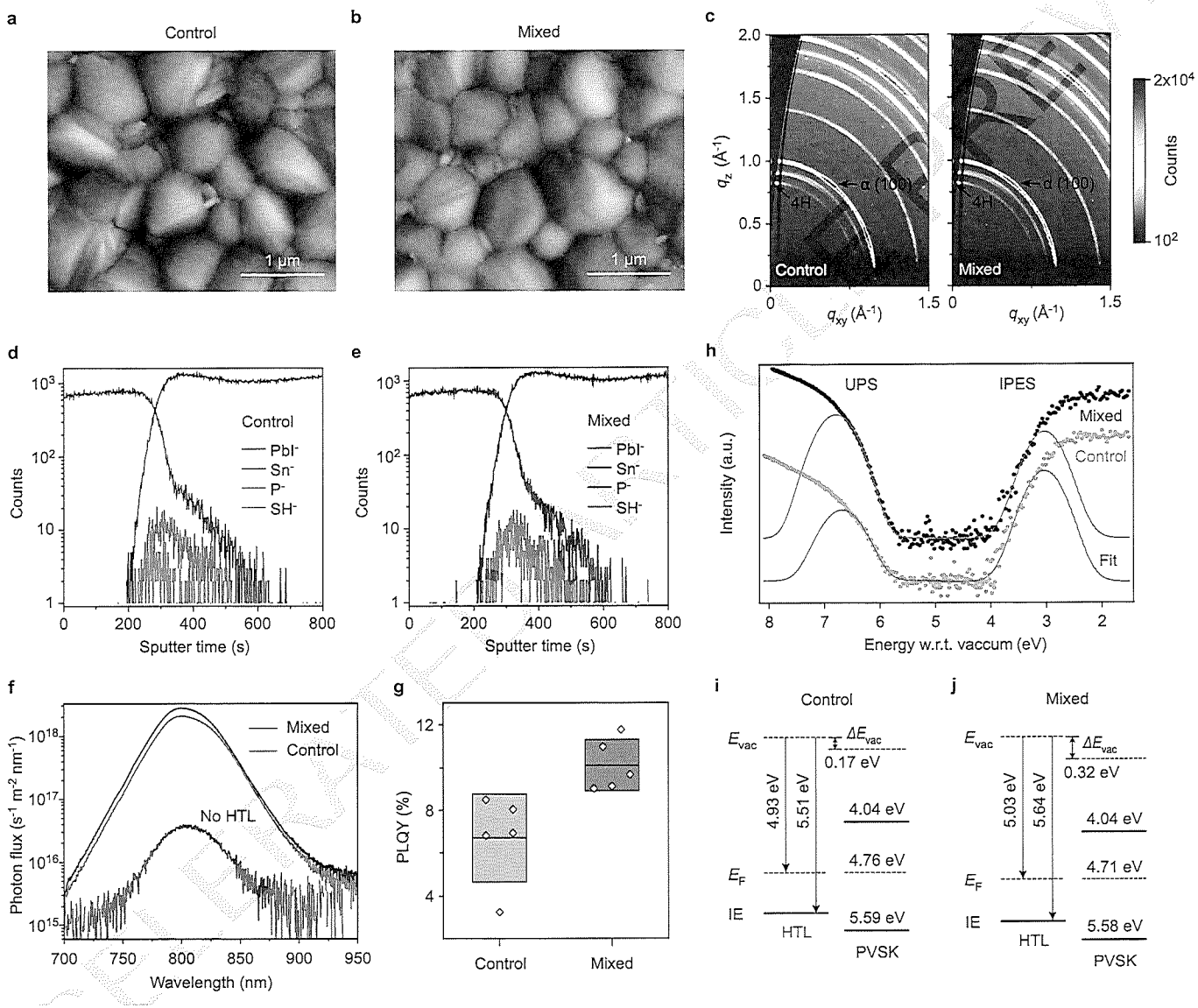
a
Control
1 µm
b
Mixed
1 µm
c
2.0
1.5
1.0
0.5
0
q_z (Å^{-1})
4H
α (100)
Control
Mixed
0
1.5
q_{xy} (Å^{-1})
2x10^4
Counts
10^2
d
10^3
10^2
10
1
Counts
Control
PbI$^-$
Sn$^-$
P$^-$
SH$^-$
0
200
400
600
800
Sputter time (s)
e
Mixed
PbI$^-$
Sn$^-$
P$^-$
SH$^-$
Sputter time (s)
h
UPS
IPES
Mixed
Control
Fit
Intensity (a.u.)
8
7
6
5
4
3
2
Energy w.r.t. vaccum (eV)
f
Mixed
Control
No HTL
Photon flux (s^{-1} m^{-2} nm^{-1})
10^{18}
10^{17}
10^{16}
10^{15}
700
750
800
850
900
950
Wavelength (nm)
g
12
8
4
PLQY (%)
Control
Mixed
i
Control
E_{vac}
ΔE_{vac}
0.17 eV
4.93 eV
5.51 eV
4.04 eV
4.76 eV
E_F
IE
5.59 eV
HTL
PVSK
j
Mixed
E_{vac}
ΔE_{vac}
0.32 eV
5.03 eV
5.64 eV
4.04 eV
4.71 eV
E_F
IE
5.58 eV
HTL
PVSK

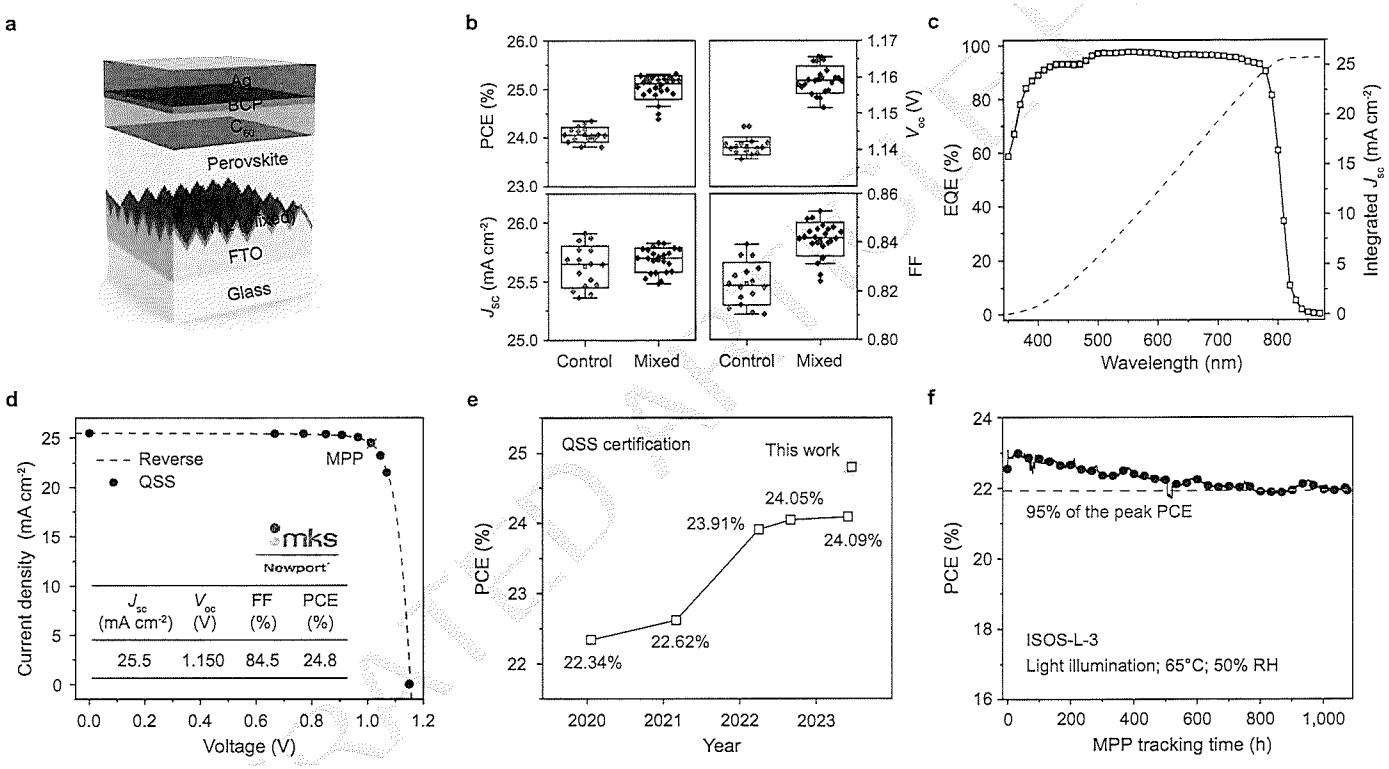
a
Ag
BCP
C60
Perovskite
Mixed
FTO
Glass
b
PCE (%)
Jsc (mA cm-2)
Voc (V)
FF
Control
Mixed
Control
Mixed
c
EQE (%)
Integrated Jsc (mA cm-2)
Wavelength (nm)
d
Current density (mA cm-2)
Voltage (V)
Reverse
QSS
MPP
mks
Newport
Jsc (mA cm-2) | Voc (V) | FF (%) | PCE (%)
25.5 | 1.150 | 84.5 | 24.8
e
QSS certification
This work
PCE (%)
Year
22.34%
22.62%
23.91%
24.05%
24.09%
f
PCE (%)
95% of the peak PCE
ISOS-L-3
Light illumination; 65°C; 50% RH
MPP tracking time (h)

nature research

Corresponding author(s): Michael Graetzel; Edward H. Sargent

Solar Cells Reporting Summary

Nature Research wishes to improve the reproducibility of the work that we publish. This form is intended for publication with all accepted papers reporting the characterization of photovoltaic devices and provides structure for consistency and transparency in reporting. Some list items might not apply to an individual manuscript, but all fields must be completed for clarity.

For further information on Nature Research policies, including our data availability policy, see Authors & Referees.

Experimental design

Please check: are the following details reported in the manuscript?

1. Dimensions

Area of the tested solar cells	☒ Yes ☐ No	0.049 cm2
Method used to determine the device area	☒ Yes ☐ No	The active area was determined by the aperture shade mask (0.049 cm2) placed in front of the solar cell

2. Current-voltage characterization

Current density-voltage (J-V) plots in both forward and backward direction	☒ Yes ☐ No	Figure 4d (reverse and quasi-steady-state scans)
Voltage scan conditions *For instance: scan direction, speed, dwell times*	☒ Yes ☐ No	Supplementary Figure 21
Test environment *For instance: characterization temperature, in air or in glove box*	☒ Yes ☐ No	Supplementary Figure 21
Protocol for preconditioning of the device before its characterization	☐ Yes ☒ No	No preconditioning is needed
Stability of the J-V characteristic *Verified with time evolution of the maximum power point or with the photocurrent at maximum power point; see ref. 7 for details.*	☒ Yes ☐ No	Supplementary Fig. 20b

3. Hysteresis or any other unusual behaviour

Description of the unusual behaviour observed during the characterization	☐ Yes ☒ No	PCE from reverse scan matches well with those from the quasi-steady-state scan and steady-state measurements.
Related experimental data	☒ Yes ☐ No	Figure 4d and Supplementary Fig. 20

4. Efficiency

External quantum efficiency (EQE) or incident photons to current efficiency (IPCE)	☒ Yes ☐ No	Figure 4c
A comparison between the integrated response under the standard reference spectrum and the response measure under the simulator	☒ Yes ☐ No	The difference was found to be less than 1.5% (Main text - Solar cell efficiency and stability)
For tandem solar cells, the bias illumination and bias voltage used for each subcell	☐ Yes ☒ No	Not relevant

5. Calibration

Light source and reference cell or sensor used for the characterization	☒ Yes ☐ No	Methods - Solar cell characterization
Confirmation that the reference cell was calibrated and certified	☒ Yes ☐ No	Methods - Solar cell characterization

Calculation of spectral mismatch between the reference cell and the devices under test	☒ Yes ☐ No	M = 1.019 for the certified device

6. Mask/aperture

Size of the mask/aperture used during testing	☒ Yes ☐ No	0.049 cm2
Variation of the measured short-circuit current density with the mask/aperture area	☐ Yes ☒ No	The accuracy of short-circuit current density was confirmed from EQE measurements.

7. Performance certification

Identity of the independent certification laboratory that confirmed the photovoltaic performance	☒ Yes ☐ No	Newport
A copy of any certificate(s) *Provide in Supplementary Information*	☒ Yes ☐ No	Supplementary Figure 21

8. Statistics

Number of solar cells tested	☒ Yes ☐ No	Figure 4b and Supplementary Figure 22
Statistical analysis of the device performance	☒ Yes ☐ No	Figure 4b and Supplementary Figure 22

9. Long-term stability analysis

Type of analysis, bias conditions and environmental conditions *For instance: illumination type, temperature, atmosphere humidity, encapsulation method, preconditioning temperature*	☒ Yes ☐ No	Figure 4f, Supplementary Figure 26 and Supplementary Figure 28